

The Upslope–Downslope Flow Transition on a Basin Sidewall

DANIEL MARTÍNEZ VILLAGRASA

University of the Balearic Islands, Palma de Mallorca, Spain and University of Utah, Salt Lake City, Utah

MANUELA LEHNER, C. DAVID WHITEMAN, AND SEBASTIAN W. HOCH

University of Utah, Salt Lake City, Utah

JOAN CUXART

University of the Balearic Islands, Palma de Mallorca, Spain

(Manuscript received 29 January 2013, in final form 24 May 2013)

ABSTRACT

The late afternoon upslope–downslope flow transition on the west inner sidewall of Arizona’s Meteor Crater, visualized by photographs of smoke dispersion, is investigated for 20 October 2006 using surface radiative and energy budget data and mean and turbulent flow profiles from three towers, two at different distances up the slope and one on the basin floor. The bowl-shaped crater allows the development of the upslope–downslope flow transition with minimal influence from larger-scale motions from outside and avoiding the upvalley–downvalley flow interactions typical of valleys. The slow downslope propagation of the shadow from the west rim causes a change in the surface radiation budget and the consequent loss of heat from the shallow atmospheric layer above the western slope at a time when the sun still heats the crater floor and the inner east sidewall. The onset of the katabatic flow is visualized by the dispersion of the smoke, and the onset occurs at the same time at the two slope towers. The katabatic flow arrives later at the crater floor, cooling the air and contributing to the stabilization of a shallow but strong inversion layer there. A wavelet analysis indicates that the initial upslope current is driven by crater-size scales, whereas the later downslope flow is influenced by the thermal gradient between opposing sidewalls generated by their different cooling rates. A comparison with other days suggests that the timing of the transition is also influenced by the presence of convective eddies in addition to the local energy balance.

1. Introduction

The reversal of daytime upslope and upvalley flows in valleys and the associated buildup of nighttime temperature inversions take place during the late afternoon and evening. The upslope–downslope flow transition, which is driven by the change in sign of the sensible heat flux on the sidewalls as they become shaded from direct solar irradiation, precedes the upvalley–downvalley transition (Whiteman et al. 1989). While the general features of the upslope–downslope transition are known, comprehensive studies of this transition that include coincident measurements of the surface radiation budget, the surface

energy budget, temperature, mean flow, and turbulence structure over the slope are scarce. An exception is a recent study by Nadeau et al. (2013) that measured radiation, turbulence, soil, and standard meteorological variables at several instrumented sites on a steep slope in a Swiss valley. In this paper, we report comprehensive observations of the upslope–downslope flow transition on a sidewall in Arizona’s Meteor Crater taken during the Meteor Crater Experiment (METCRAX) in October 2006 (Whiteman et al. 2008). The transition on the east-facing sidewall of the Meteor Crater develops differently than the transition observed by Nadeau et al. (2013) on a west-facing slope because of differences in shadow propagation along the slope.

During the evening of 20 October 2006, the slope flow reversal on the west inner sidewall was visualized by time-lapse movies of smoke dispersion from three consecutive smoke releases from a site in the middle of the

Corresponding author address: Daniel Martínez Villagrasa, Zentrum für Angewandte Geowissenschaften, Eberhard Karls Universität Tübingen, Hölderlinstr. 12, 72074 Tübingen, Germany.
E-mail: daniel.martinez@uni-tuebingen.de

sidewall (Fig. 2). The processes producing the upslope–downslope flow transition and the sequence of events are the subject of the present paper.

The following section describes previous research on the upslope–downslope flow transition, while the description of the METCRAX sites and data are introduced in section 3. General characteristics of the case study are given in section 4, and the features of the observed flow transition are presented in section 5. In sections 6 and 7, the results from the case study are further discussed and compared to the transition on several other days. Conclusions are presented in section 8.

2. Background

Drainage flows develop during stable conditions over most land surfaces, even over those with very small slope angles, under clear skies and weak synoptic background flows. They have been studied in many different locations, including Antarctica (Renfrew 2004) and Greenland (Heinemann 2002), as well as in different topographies of midlatitudes (Haiden and Whiteman 2005; Cuxart et al. 2007; Papadopoulos et al. 1997, and others). Drainage flows have been addressed analytically by simplifying the set of equations that describe the flows (Prandtl 1942; Fleagle 1950; McNider 1982) or numerically (Manins and Sawford 1979). Others have compared the simple solutions with experimental results (Mahrt 1982; Haiden and Whiteman 2005) or against mesoscale simulations of real cases (Martínez and Cuxart 2009). For a complete review see Zardi and Whiteman (2012).

The onset of katabatic flow in the evening has been addressed through observations on relatively homogeneous and gentle slopes. The details of the initial stage depend on both the terrain features and ambient conditions. In the absence of any opposing motion, the downslope flow develops gradually with the formation of a temperature inversion through surface cooling (Papadopoulos and Helmis 1999). When a slope is oriented toward the east with increasing inclination in the upslope direction, a shadow starts to cover the surface from the upper part of the slope where the air first becomes stably stratified. In these cases, the drainage flow begins at the upper shaded part of the slope and its subsequent arrival farther downslope may occur in the form of a propagating gravity current (Papadopoulos and Helmis 1999; Mahrt et al. 2010). At a given point on the lower slope, the arrival of the gravity current is characterized by a sudden shift in wind direction and a temperature drop (Simpson 1999).

When there is an opposing flow (either an anabatic current or a larger-scale flow), the local surface cooling generates the buoyancy conditions that lead to the onset

of a gravity current once the opposing flow disappears. Mahrt and Larsen (1982) found that an opposing larger-scale flow delayed the onset of a drainage current for several hours. It then appeared in the form of a gravity current with a thick frontal bulge. Sometimes, the gravity current arrival occurs only with a sudden wind shift, while the temperature decreases gradually (Monti et al. 2002) or simply increases the cooling rate (Mahrt et al. 2010).

Beginning with an existing anabatic current, Hunt et al. (2003) developed a simplified theoretical model to describe the upslope to downslope transition over a gentle slope. The transition occurs via the formation of a stagnant frontal region (see their Fig. 3) at a certain distance upslope. This distance depends on the initial buoyancy, the cooling time scale of the surface layer and the former upslope velocity. Results from a laboratory experiment supported the theoretical predictions. Monti et al. (2002) and Brazel et al. (2005) used guidance from the simplified model to analyze their wind transitions, while Mahrt et al. (2010) report that a period of weak winds and variable directions occurs following the cessation of the upslope flow before the katabatic current begins. Nadeau et al. (2013) also observed a short period of calm winds before the onset of the downslope flow. But in contrast to the model by Hunt et al. (2003) their observations in a Swiss valley showed a transition front that moved up the slope instead of down the slope. This is explained by the upward propagation of the evening shadow or local sunset on the steep west-facing slope, thus highlighting the importance of the direction of shadow propagation on the upslope–downslope flow transition. Recent observations from Fernando et al. (2013) over a more complex area support the front formation model, where the arrival of multiple fronts from different slopes during the evening transition extends the transient period before the downslope flow ensues.

The flow transition for slopes on valley sidewalls is necessarily embedded in the larger-scale along-valley circulations and their corresponding compensating return motions in the upper part of the valley atmosphere (Whiteman 2000). As an example, see the results from a large-eddy simulation of a complete diurnal cycle of the thermally driven circulation over an idealized valley performed by Catalano and Cenedese (2010). Nadeau et al. (2013) observed a transition from upvalley to downslope flow on many evenings instead of a transition from upslope to downslope flow. During the day, the upslope wind is modulated by its interaction with the convective boundary layer evolution within the valley atmosphere (Serafin and Zardi 2010). At night, the downslope current either is affected by the growth of a cold pool at the base of the slope (Cuxart et al. 2007; Zhong and Whiteman 2008) in the case of an enclosed

basin, or interacts with the downvalley current (Whiteman et al. 1989). In an enclosed basin like the Meteor Crater, however, the transition from daytime upslope to nighttime downslope flows can be studied without the complicating factor of the along-valley wind circulation. The basin topography thus allows one to focus on key mechanisms of the slope-flow transition.

In enclosed basins of a size similar to the Meteor Crater, the onset of drainage flows is produced after the reversal of the sensible heat flux (Whiteman et al. 1989). The slope currents can be generated locally, persisting until the growth of the cold pool eliminates the temperature differences between the air close to the sidewall and the air at the same level over the center of the basin (Clements et al. 2003) or can be generated by an inflow of colder air into the basin (Fast et al. 1996; Whiteman et al. 2010).

3. Meteor Crater topography and meteorological data

Arizona's Meteor Crater (Fig. 1), 40 km east of Flagstaff, Arizona, was produced by the impact of an approximately 50-m-diameter meteorite about 50 000 years ago (Kring 2007). The nearly rotationally symmetric, bowl-shaped basin is 170 m in depth and has a diameter of 1.2 km, with an unbroken rim that extends 30–60 m above the surrounding arid uniform plain that slopes gently upward to the southwest of the crater. The soil inside the crater becomes increasingly rockier with distance up the alluvium on the sidewalls and is sparsely covered with grasses and small bushes.

The meteorological equipment and accuracies, measurement locations and other details of the METCRAX experimental program were summarized by Whiteman et al. (2008). Here, a brief overview of the measurements used in the present article is provided. The primary data come from an array of five 10-m micrometeorological flux towers located on an east–west cross section inside the crater (Fig. 2). They were installed near the center of the crater floor (FLR), on the lower-west (WL) and upper-west (WU) sidewalls, and on the lower-east (EL) and upper-east (EU) sidewalls. The corresponding slope angles are 0°, 4°, 22°, 7°, and 24°, respectively. The measurement equipment on the flux towers is listed in Table 1. GPS receivers at each of the towers provided accurate time registration of the individual datasets. Sonic anemometers were installed vertically and the data were rotated into a mean wind-following coordinate system using the planar-fit method of Wilczak et al. (2001). All components of the surface radiation budget were individually measured at these sites over a surface parallel to the local slope (see Hoch and Whiteman 2010



FIG. 1. Aerial photograph of Meteor Crater from the southeast. The photograph was taken on the morning of 14 Jul 1958 (copyright J. S. Shelton, used with permission).

for more details). The sensible and latent heat fluxes were calculated by the National Center for Atmospheric Research Earth Observing Laboratory's Integrated Surface Flux System correcting the sonic temperature for water vapor effects (Schotanus et al. 1983), the hygrometer measurements for UV absorption by oxygen (van Dijk et al. 2003), the water vapor flux following Webb et al. (1980), and for the spatial separation of the sonic anemometers and the hygrometers (Horst and Lenschow 2009). In addition, a 10-m tripod was located at the highest point on the crater rim (RIM) measuring averaged meteorological data at 2 and 10 m. The data used in this study have been averaged over 5-min and 30-s periods. The difficulty in choosing an appropriate averaging period is that the size of the largest turbulent eddies changes strongly during the upslope–downslope flow transition and that there is a need for high temporal resolution of the fast changing transition. An averaging period of 5 min for turbulent fluxes during the upslope–downslope flow transition was also used by Nadeau et al. (2013).

Three tether sondes were operated simultaneously along the same east–west cross section on the west sidewall (TS-W), floor (TS-C), and east sidewall (TS-E). They provided vertical profiles of meteorological variables within the depth of the crater atmosphere at approximately 30-min time intervals during 7 intensive observational periods (IOPs). Additionally, for the present case study (IOP 4 on 20 October 2006) the slope flow reversal on the west sidewall was visualized by time-lapse movies of smoke dispersion from a site 50 m south of WU (Fig. 2).

4. Case study of 20 October 2006

The upslope–downslope flow transition took place on the west sidewall of the crater between 1500 and 1600

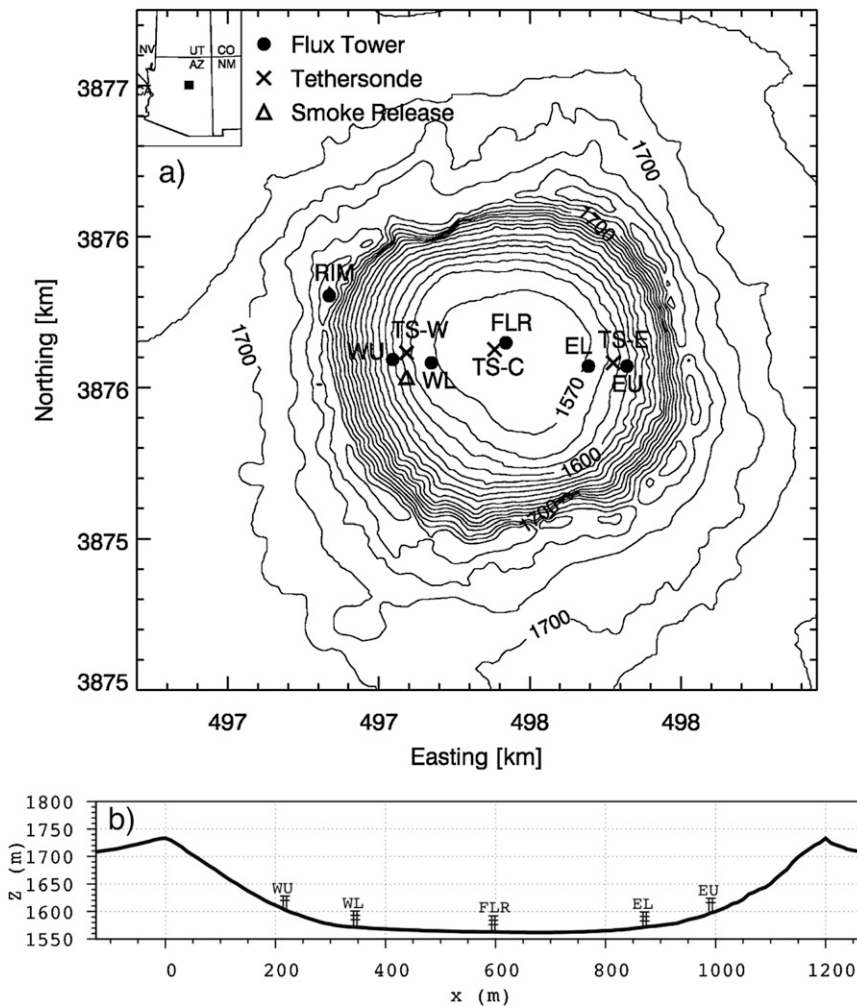


FIG. 2. Location of meteorological instrumentation in Arizona's Meteor Crater and its surroundings. (a) Universal transverse Mercator zone 12S map with altitude contours every 10 m. Flux towers are indicated with black dots and are labeled WU, WL, FLR, EL, EU, and RIM. Tethered balloon sounding locations are indicated with times signs as TS-W, TS-C, and TS-E. The three smoke releases were made at the point indicated with a triangle. (b) Topographic cross section of the crater showing the locations of WU, WL, FLR, EL, and EU.

Mountain standard time (MST). This transition will be analyzed in the following sections. The afternoon and early evening period was characterized by clear, undisturbed meteorological conditions. Clear skies and light and variable winds persisted until the arrival of a weak cold front from the northwest at approximately 2100 MST. Winds gradually increased after astronomical sunset (1732 MST) and shifted from northeasterly to southwesterly on the surrounding plain. Winds at the crater rim remained below 5 m s^{-1} until after astronomical sunset, a speed threshold considered by Yao and Zhong (2009) to separate decoupled from coupled conditions at Meteor Crater.

The upslope–downslope flow transition within the crater basin is strongly affected by the propagation of shadows cast by the crater rim, which blocks incoming shortwave radiation well before astronomical sunset. Figure 3 shows the modeled propagation of shadows for selected times during the evening of 15 October. The inner southwest sidewall of the crater is the first area covered by shadow. Similarly, the northeast inner sidewall is the area of the crater that receives the largest amount of irradiance in the late afternoon. This configuration establishes a horizontal gradient of irradiance following a northeast–southwest orientation. This gradient contributes to the dynamics within the crater (Lehner

TABLE 1. Meteorological measurement equipment at the micrometeorological flux towers.

Instrumentation	Sampling interval (Hz)	Averaging interval	Heights (m) at WU-EU	Heights (m) at WL-EL	Heights (m) at FLR
Sonic anemometers	20	30 s, 5 min	0.5, 1.5, 3.0, 5.0	0.5, 1.5, 3.0, 5.0, 8.5	0.5, 2.0, 5.0, 8.5
UV absorption hygrometer	20	30 s, 5 min	3.0	3.0	3.0
Hygrothermometers	1	1 min	0.5, 1.5, 3.0, 5.0	0.5, 1.5, 3.0, 5.0, 8.5	0.5, 2.0, 5.0, 8.5
Soil radiation thermometer	1	1 min			
Barometer	1	1 min	2.0	2.0	2.0
Slope-parallel four-component radiometers	0.2	1 min	2.0	2.0	2.0
Soil temperature, soil thermal properties, soil heat flux, soil moisture	0.2	5 min	-0.05	-0.05	-0.05

et al. 2011). As the sun sets, the shadow moves north-eastward down the west sidewall and across the floor of the crater. Local sunset arrives 160, 130, 75, 55, and 40 min before astronomical sunset at the WU, WL, FLR, EL, and EU sites, respectively (Hoch and Whiteman 2010).

The effects on the stratification of the crater atmosphere of the shadow propagation can be analyzed through vertical profiles from the three tether sondes collected in the late afternoon and evening (Fig. 4). For the sake of brevity, potential temperature will be simply referred to as temperature hereinafter. The time evolution of the temperature profiles shows the development of a stable layer at the lower elevations within the crater, starting at the western side of the crater, as wind speed

continuously decreases within the crater atmosphere because of the decoupling from the ambient flow aloft (not shown). At 1601 MST, when the shadow covers almost half of the crater, the stability has built up over the west sidewall, while the temperature profile remains superadiabatic at the crater floor and over the eastern part. Temperature differences develop across the crater, with a difference of about 0.5 K in the upper crater atmosphere between the west and east tether sonde sites. At 1701 MST, when the shadow covers almost the entire crater, the temperature profile differences are minimized. A strong inversion of 5 K in the first 50 m is formed over the crater floor by the time of astronomical sunset. From this time on, the wind aloft veers to the

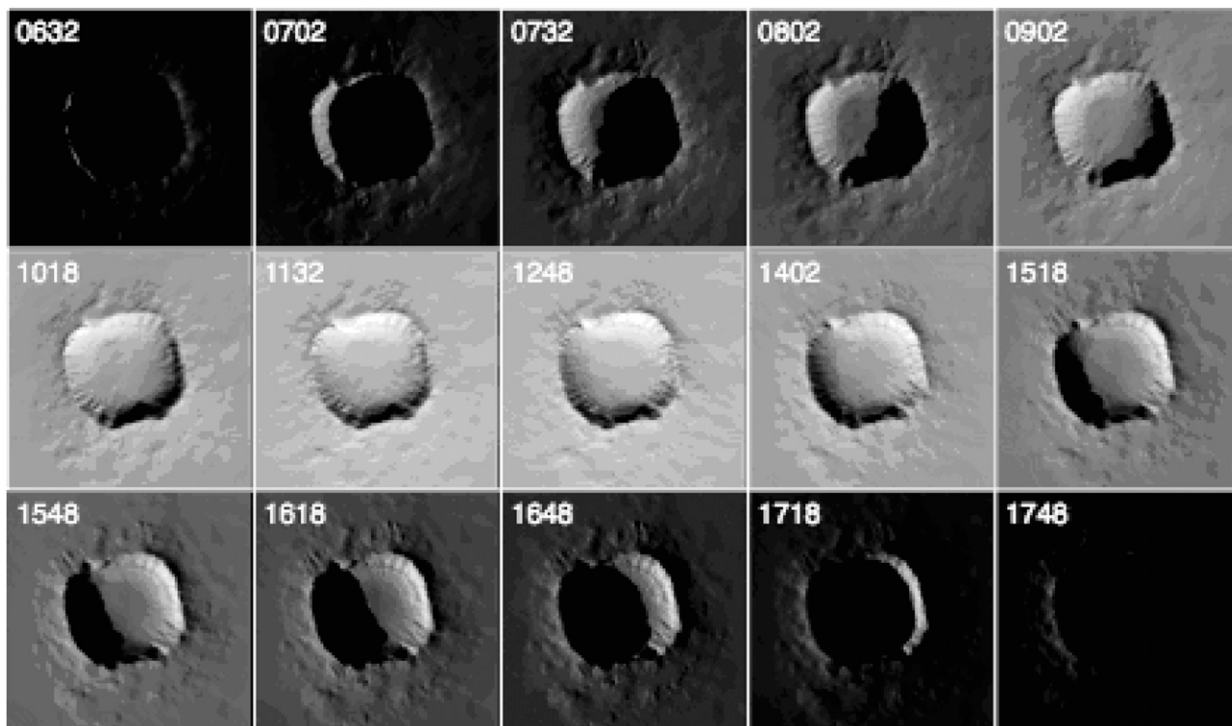


FIG. 3. Modeled propagation of shadows and extraterrestrial insolation across the Meteor Crater on 15 Oct at different times of day (MST). Shades of gray are radiation intensity with black indicating 0 and white indicating 1364 W m^{-2} .

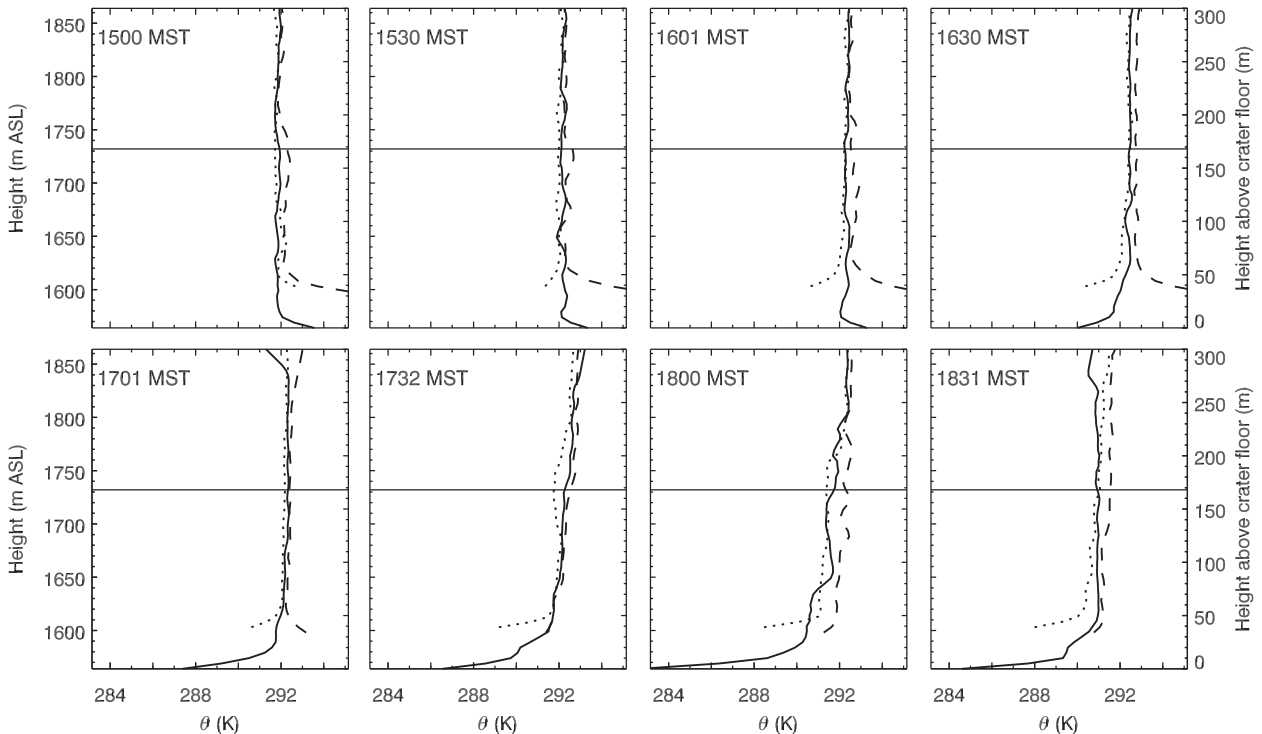


FIG. 4. Potential temperature profiles on the western sidewall (dotted), crater floor (solid), and eastern sidewall (dashed) from 1500 to 1831 MST. Tethered balloon soundings above 20 m AGL are complemented with near-surface temperature profiles from WU, FLR, and EU. A three-point smoother was applied to the profiles after interpolating the data to heights at 5-m intervals. Sounding times are indicated in the top-left corner. The solid horizontal line indicates the mean crater rim level. Local sunsets at the crater floor and the east sidewall sounding sites were at 1606 and 1645 MST on 22 Oct, respectively, with local sunset at the tower sites occurring 2–3 min later on 20 Oct than on 22 Oct. Local sunset at the west sidewall sounding site was at approximately 1528 MST based on shortwave radiation measurements at WU and WL.

west and increases in speed as the cold front approaches (not shown). This wind speed increase is transported downward at the eastern part of the crater, where turbulent eddies mix the air downward here (Yao and Zhong 2009). Such wind speed increase does not affect the western part, however, presumably because it is dynamically sheltered by the upwind rim, which blocks the wind blowing from the west. This situation leads to a faster cooling of the western part of the crater during this period.

5. The upslope–downslope flow transition

a. Smoke dispersion

Three 3-min-duration smoke releases were made at a site on the west sidewall at 1510, 1530, and 1550 MST as the shadows propagated down the slope (Clements et al. 2007). Time-lapse photographs recorded the dispersion of the plumes generated by the smoke releases. Figure 5 shows one picture representative of each smoke release.

The first smoke release occurred when the shadow edge (the terminator) had just passed WU and the smoke release site. Upslope easterly winds were still present

over the shadowed slope, with big eddies that were able to transport the smoke up to the rim (Fig. 5a).

The second release was made just after the terminator passed WL. At this time, the slope flow intermittently reversed from downslope to upslope and from upslope to downslope (Fig. 5b). The downslope flow confined the smoke plume to the ground, while it was dispersed vertically by the enhanced turbulence when the flow turned upslope.

The third smoke release took place when the shadow covered the entire west sidewall, as shown in Fig. 3. At this time, the smoke plume propagated downslope in a shallow layer whose depth increased along the slope (Fig. 5c). The time-lapse movie showed that the flow was disturbed occasionally by turbulent episodes that sporadically dispersed the smoke plume vertically, reaching a height of tens of meters above ground level (AGL). When the smoke plume was observed from the east sidewall (Fig. 5d), this perspective revealed that the downslope current blew from the southwest, with the smoke flowing between the two west slope towers with a depth similar to the height of the WL tower. Part of the

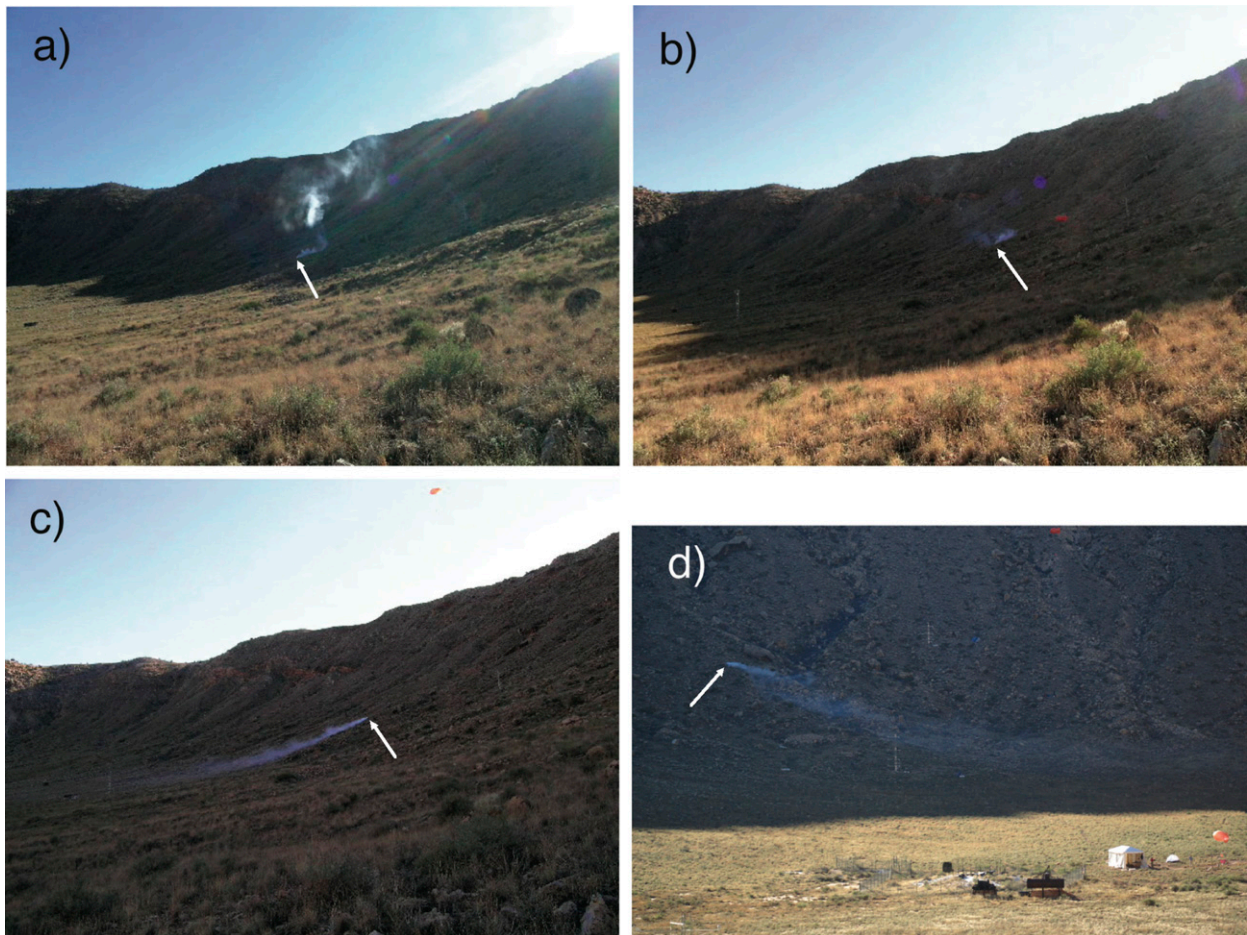


FIG. 5. Photographs of the dispersion of smoke from 3-min-duration releases on the west slope of Meteor Crater started at (a) 1510, (b) 1530, and (c) 1550 MST 20 Oct 2006, as photographed from a point on the crater floor northeast of the smoke release. (d) As in (c), but photograph was taken from the foot of the east sidewall. The white arrows indicate the locations of smoke releases. The WU and WL towers can somewhat be seen in the photographs. A red tethered balloon is slightly visible in (b).

smoke arrived at the crater floor detached from the surface (not shown). At this time FLR was still illuminated by the sun, with a thin unstable layer close to the surface and neutral or weakly stable stratification above 10 m AGL (Fig. 4; 1601 MST). The weakly stable layer prevented the smoke from reaching the surface. The perspectives of the photographs, however, were such that it is unclear whether smoke reached the FLR site where the ground-based unstable layer was observed.

b. Results from the meteorological towers

Figure 6 shows data from the WU and WL sites averaged over 5-min intervals during the upslope–downslope flow transition visualized by the smoke releases. The 30-min delay in shadow arrival between the two west sidewall sites leads to different surface conditions during the transition period.

Net radiation changes sign abruptly with the passage of the terminator because of the large shortwave radiation drop (Figs. 6a,b). This drop of net radiation is larger at WL since global radiation is larger when the shadow arrives at this site because of its gentler slope angle (Hoch and Whiteman 2010). The sudden lack of shortwave energy input that had warmed the surface results in a rapid decrease in the temperature. The associated decrease in the radiating temperature of the surface is indicated by the immediate decrease in the magnitude of the outgoing longwave flux. This decrease in the outgoing longwave radiation is larger at WL than at WU, corresponding to the relative magnitudes of the change in shortwave available energy.

Figures 6c and 6d show the response of the other components of the surface energy balance to the sudden decrease in net radiation. The sign convention used in

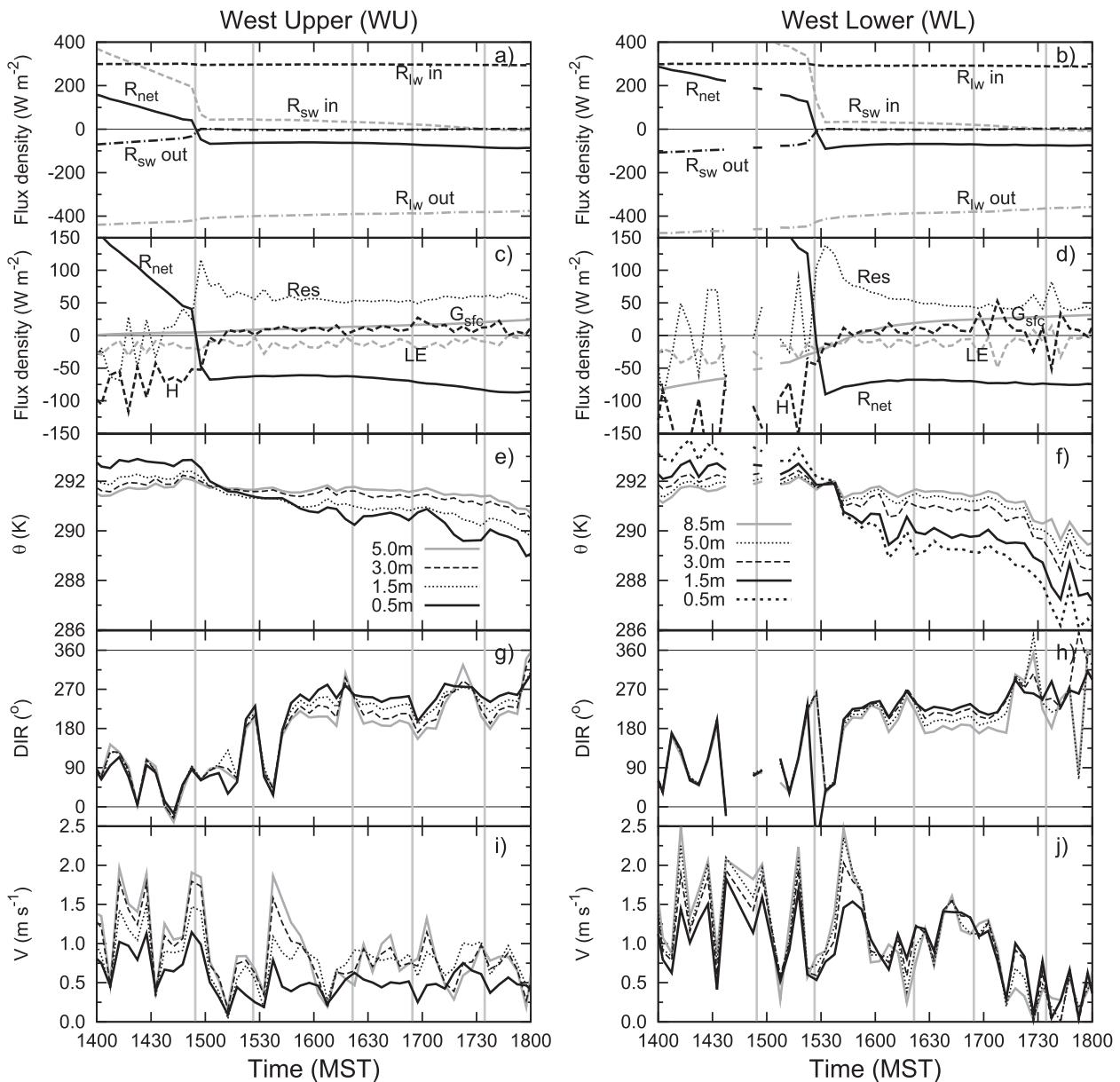


FIG. 6. Meteorograms from the (left) WU and (right) WL towers for the evening period of 20 Oct 2006. (a),(b) Radiation budget components at 2 m AGL; (c),(d) surface energy budget components, including net radiation R_{net} , surface heat flux G_{sfc} , sensible heat flux H and latent heat flux LE at 3 m AGL, and energy balance residual $Res + R_{\text{net}} + G_{\text{sfc}} + H + LE = 0$; (e),(f) potential temperature; (g),(h) wind direction and (i),(j) wind speed at different levels of the towers. Data are from 5-min averages. Vertical lines indicate the times of local sunset at from left to right WU, WL, FLR, and EU and astronomical sunset (extreme right).

this study is that fluxes directed toward the surface, whether from the atmosphere or soil, are positive. The sensible heat flux at 3 m AGL reverses approximately 15 min after the shadow passage at both sites, while the latent heat flux remains small and negative during the whole upslope–downslope flow transition, indicating sustained evaporation. Soil moisture on 20 October was low since the last rain at the crater occurred two weeks

before this IOP. Large differences can be seen in the evolution of the ground heat fluxes at the different sites. At WL the ground heat flux shows a strong reaction to the change in net radiation at approximately the same time as sensible heat flux. At WU, however, the ground heat flux reverses well before local sunset, growing only from 0 to 25 W m^{-2} between 1400 and 1800 MST, while the ground heat flux at WL changes from -85 to $+30 \text{ W m}^{-2}$.

Local irregularities of the terrain and scattered bushes could shade the ground effectively before local sunset at WU, where a steeper slope leads to longer shadows. This effect, together with differences in the soil thermal characteristics with distance up the alluvium on the sidewalls, could be an explanation for the differences between the two west slope sites. Further, the ground heat flux is determined as the sum of a measured flux from a heat flux plate at a certain depth and the change in heat storage in the soil above the plate. Depending on the depth and thermal properties of the soil above the flux plate and the representativeness of the soil temperature measurements, sudden flux changes directly at the surface cannot be resolved in the observations and appear as a smoothed-out signal. The measured imbalance of the surface energy budget [see additional information on this feature, which is seen in many measurement programs, in Oncley et al. (2007)] is very large, especially immediately after local sunset. The slow response time of the ground heat flux measurements may be responsible for the especially large imbalances around local sunset.

Figures 6e and 6f show the local potential temperature, defined here by $\theta = T + \Gamma_D \delta z$, where $\Gamma_D \approx 0.0098 \text{ K m}^{-1}$ is the adiabatic lapse rate and δz is the relative elevation above the crater floor. The near-surface air temperature decreases following the passage of the terminator, as it is strongly influenced by the ground surface temperature. Similarly to the drop in surface temperature, the air temperature drop at WL at local sunset is larger than at WU. The near-surface cooling of air stabilizes the surface layer, and results in the reversal of sensible heat flux (Figs. 6c,d).

Wind direction evolves simultaneously at both sites (Figs. 6g,h) and mirrors the evolution of the observed smoke plumes. The wind shifts from the easterly upslope direction observed with the 1510 MST smoke release into a southwesterly downslope direction by the time of the third smoke release. Wind directions are variable from about 1515 to 1540 MST during the second smoke release. By the time of the third smoke release at 1550 MST, a steady downslope current has been established. This current persists for the next two hours, although with two mixing episodes and with wind speeds significantly lower than for the upslope regime (Figs. 6i, j). The downslope current presents a layered structure with a westerly to southwesterly direction close to the surface, progressively turning into a southerly direction with height. This wind direction shear is largest for WU.

To compare the flow evolution among sites, Fig. 7 shows the 30-s-averaged wind speeds and directions for the WU and WL (3 m AGL) and FLR (2 m AGL) towers, together with the local 1-min-averaged potential temperatures at two different heights for each tower.

The wind direction at WL turns suddenly into 180° at 1538 MST (gray arrow in Fig. 7b), which marks the onset of the downslope current, and then gradually changes to a southwesterly direction over the next 10 min (1550 MST). The same evolution is seen at WU with a delay of two minutes. With the downslope regime established, the wind direction remains more or less steady until 1710 MST with a similar evolution at both west sidewall sites. The period from 1540 to 1710 MST will thus be referred to as the downslope regime.

At WU the temperature close to the surface (1.5 m AGL) decreases quickly in the first 20 min after local sunset (1454 MST). The temperature at 5 m AGL, however, remains similar to that recorded at RIM. This indicates that the buildup of the stable layer is formed by surface cooling and is confined to the first 5 m AGL. At WL, the buildup of stability and a sudden drop of temperature in the whole column coincide with the final onset of the downslope current (1538 MST). Before this event, there is another significant drop in air temperature when the flow suddenly changes into a downslope direction for nearly 8 min (around 1525 MST). With the final establishment of the downslope current, the 5-m AGL temperatures at WU and WL drop below the temperature at RIM, indicating the formation of a weak surface-based inversion over the western sidewall of the crater. These temperatures remain approximately steady until 1710 MST when the buildup of the cold pool within the basin leads to a decrease of both temperature and wind speed that is larger at WL (Fig. 6), anticipating the end of the downslope regime.

At FLR, the air temperature starts to decrease with the arrival of air from the west sidewall (dashed arrow in Fig. 7b) 10 min after the onset of the downslope current at WL and about 30 min before local sunset. This shows the importance of the contribution of the katabatic flow to the cooling of the lower atmosphere over the basin center. However, the largest temperature drop occurs after the arrival of the terminator at FLR (1622 MST). The surface cooling associated with the shadow passage increases atmospheric stability close to the surface. Nevertheless, a weak downslope current is able to continue to reach the FLR site (Fig. 7a).

c. Evolution as seen by the wavelet transform

A wavelet analysis of the kinetic energy (KE) as measured by the sonic anemometers on the towers was performed to identify the relevant scales of motion during the upslope–downslope flow transition. The wavelet transform is a spectral tool conceptually equivalent to a local Fourier decomposition that characterizes non-stationary time series of any magnitude with different temporal scales (Viana et al. 2009). In this study, the

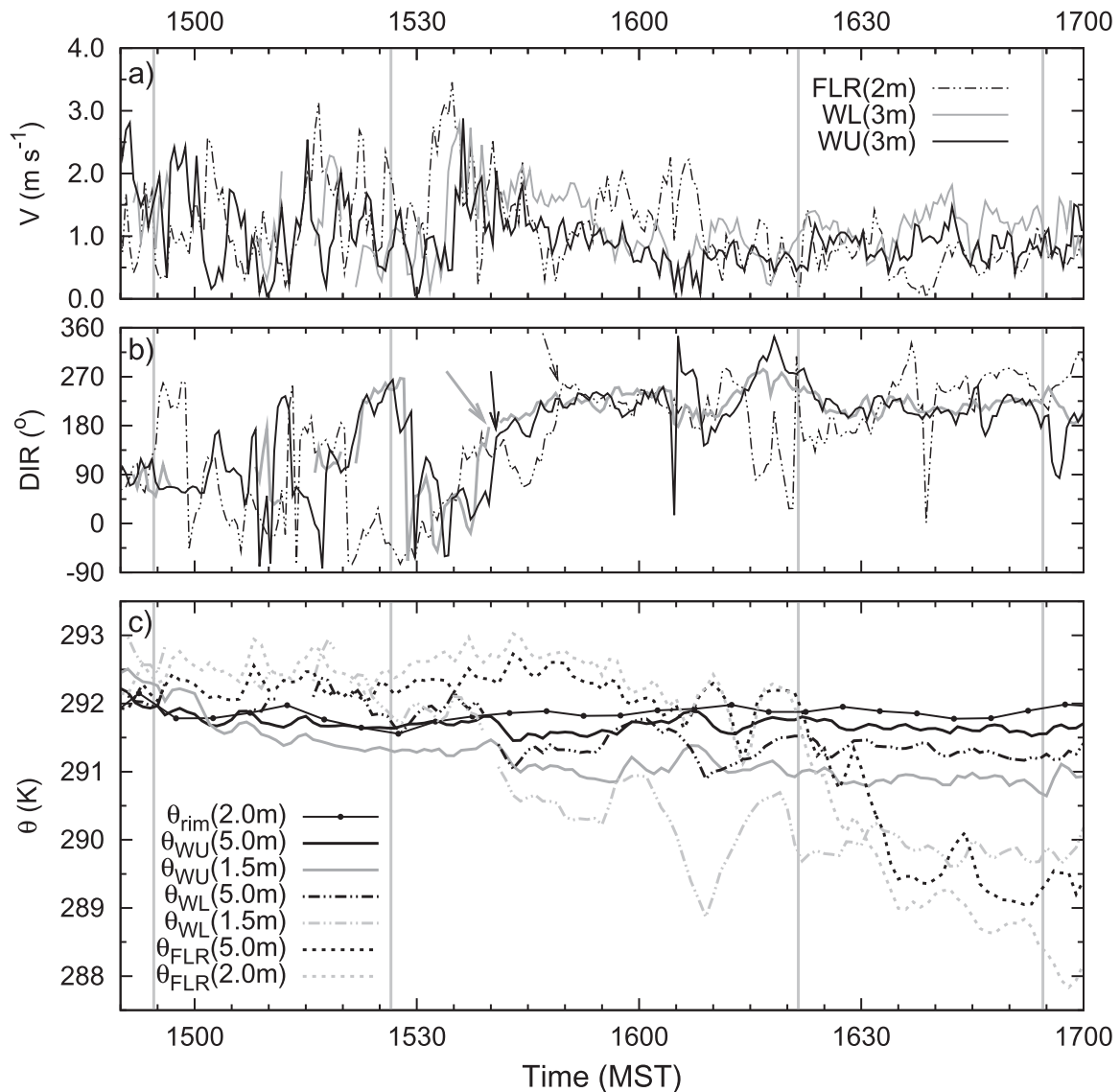


FIG. 7. Time evolution of (a) wind speed, (b) wind direction, and (c) local potential temperature for the WU, WL, and FLR sites. Wind and temperature data correspond to 30-s and 1-min averages, respectively. In (c), the 5-min-average local potential temperature measured at the rim is shown for comparison. Vertical lines indicate the times of local sunset at left to right WU, WL, FLR, and EU. In (b), arrows indicate the arrival of the gravity current at WL (thick gray), WU (solid black) and FLR (dashed).

Morlet wavelet with a nondimensional base frequency w_0 of 6 has been applied to 20-Hz wind components and virtual temperature time series. The Morlet function has the advantage of relating the temporal scales to equivalent Fourier periods (Meyers et al. 1993) and has been widely used for the analysis of geophysical time series (Cuxart et al. 2002; Viana et al. 2010).

The decay of turbulence during the evening transition in the convective surface layer is usually described in terms of the evolution of the turbulence kinetic energy (TKE), which responds to the weakening of the surface sensible heat flux as solar radiation decreases. Previous

studies over flat terrain indicate that TKE initially decays slowly when sensible heat flux starts to decrease (Sorbján 1997; Nadeau et al. 2011). This period is followed by an abrupt decay just before sunset when the surface heat flux becomes negative. Over complex terrain, TKE could be expected to decay faster because of the rapidly evolving surface radiation budget produced by the presence of shadows (Nadeau et al. 2013).

For illustrative purposes, Fig. 8 shows the wavelet transform of the KE time series recorded at 5 m at WU. Wavelet transforms were also calculated for WL and FLR (not shown). At all sites, the relevant wavelet

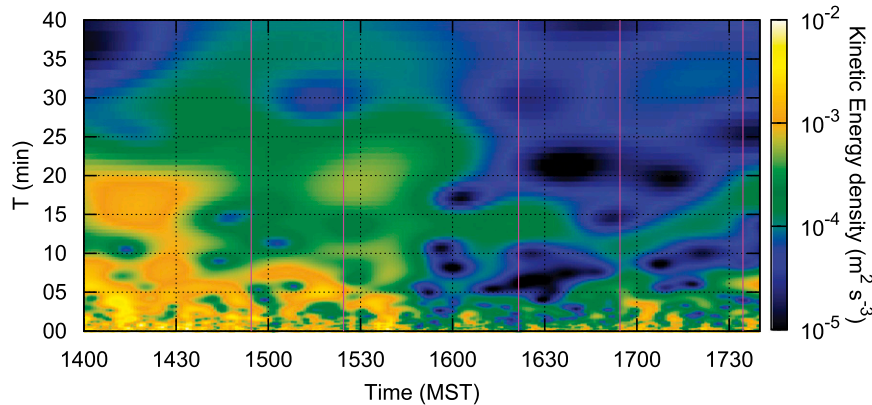


FIG. 8. Time evolution of KE per unit period at 5-m height computed from the wavelet transform of the wind components at WU. Vertical lines are as in Fig. 6.

scales (here, represented by the equivalent Fourier periods T) that contribute to the KE decrease with the onset of the drainage flow from time scales of up to 25 min to time scales below 15 min. Assuming Taylor's hypothesis and a horizontal velocity scale of 1 m s^{-1} , the resulting maximum daytime length scale is 1500 m, a value that can be related to the crater scale. Lehner and Whiteman (2012) performed large-eddy simulations of thermally driven cross-basin winds during daytime in an idealized, closed basin based on the Meteor Crater topography. Their study shows that the surface thermal asymmetry leads to the formation of a closed circulation cell within the crater. Depending on the background-wind direction with respect to the temperature gradient, this rotating cell encompasses sizes up to the basin scale. An idealized circular cell whose circumference is 1500 m corresponds to a circle with a diameter of approximately 500 m, a length compatible with the size of cells developed in their simulations.

A short time prior to local sunset at WU, the larger scales ($T > 10$ min) lose intensity and vanish rapidly with the onset of the drainage flow. During the downslope regime (1540–1710 MST), the most intense scales are confined below 5 min while a second maximum remains around 12 min, with a gap separating these two regions in the temporal scale domain. The smaller time scales are related to turbulent motions and contribute to the TKE. Similarly, after assuming Taylor's hypothesis and a horizontal velocity scale of 1 m s^{-1} , the larger scales correspond to lengths scales of 600–900 m, half the size of the crater. At FLR, the gap is not present (not shown), probably because the center of the crater floor is influenced by phenomena of a wider range of scales generated at other parts of the basin.

To sum up these results for the three towers, the energy has been integrated between two periods, (i) the

turbulent periods (0–5 min) and (ii) larger-scale periods (5–40 min). The time evolution of both contributions (Fig. 9) shows clearly the two regimes present. During the upslope regime (up to 1538 MST), the KE for both turbulent and larger periods is at least twice as large as during the downslope regime (1540–1710 MST).

The KE decay is produced at a slow rate during the upslope regime, governed by the local evolution of surface heat flux as described by Nadeau et al. (2011). However, the following abrupt decrease is produced with the onset of the downslope flow at all sites and is disconnected from the rapid evolution of the surface radiation budget around local sunset, in contrast to Nadeau et al. (2013). For all sites, the change of regime is preceded by an enhanced peak of small-scale turbulence or TKE. The contribution of TKE to kinetic energy even exceeds that of the larger-scale contributions at WU and WL. This peak coincides with a sudden increase of wind speed (1532–1537 MST, Fig. 7a) and occurs at nearly the same time at all three sites and at EL (not shown), indicating that the event occurs practically throughout the entire crater. Moreover, this energy enhancement takes place at all periods up to 25 min, suggesting that the event has a crater scale. With the establishment of the downslope flow the contribution of the larger scales progressively decreases until reaching values similar to those for TKE. Goulart et al. (2010) show that shear production of TKE can enhance the decay time scale. Here wind shear cannot be neglected during the upslope–downslope flow transition (Figs. 6g–j), in contrast to the observations of Nadeau et al. (2013). The mechanical production of TKE probably plays an important role in the turbulence evolution, contributing to the slow decay of KE during the upslope regime and producing the TKE during the downslope regime.

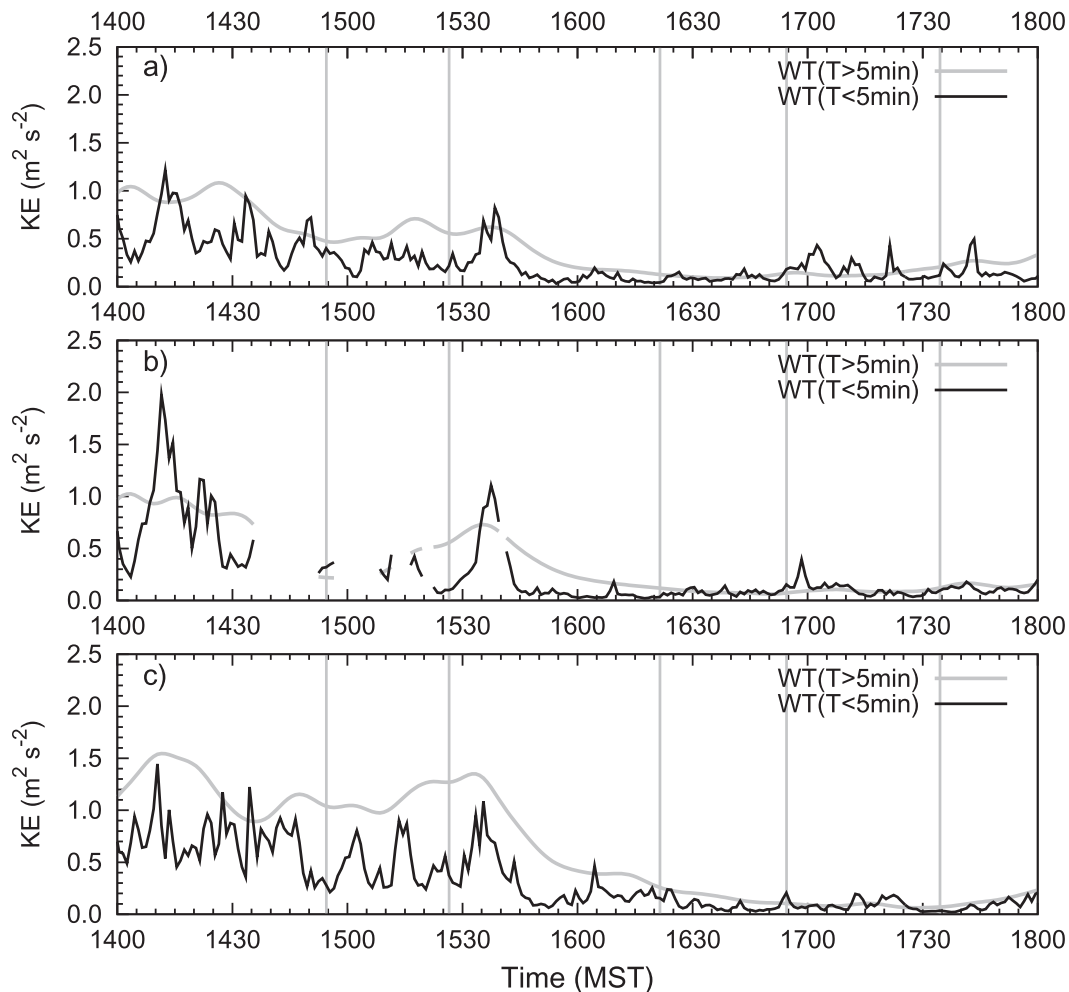


FIG. 9. Time evolution of the contribution to KE at 5-m height at small periods (up to 5 min), and at longer periods for the (a) WU, (b) WL, and (c) FLR sites. The scale contribution has been computed from the wavelet transform of the wind components (see text for more details). Contributions of periods below 5 min are considered representative of turbulence scales. Vertical lines are as in Fig. 6.

6. Discussion of the flow dynamics and thermodynamics

The upslope–downslope flow transition at the inner-west sidewall of the crater is related to the propagation of the shadow cast by the west rim, which descends the slope as the sun gets lower in the sky in late afternoon. The ground surface cools rapidly after the arrival of the shadow edge. The sensible heat flux close to the ground diminishes and then changes sign, leading to a downward heat flux that cools the atmosphere above the slope and leads to the buildup of a surface-based temperature inversion. Neither the downward sensible heat flux nor the observed ground heat flux are large enough to compensate for the negative net radiation, which leads to the large imbalances in the measured surface energy budget (Figs. 6c,d).

Parts of the energy imbalance can be related to sensible heat and radiative flux divergences between the ground and the respective 3- and 2-m AGL heights where these fluxes were recorded (Oncley et al. 2007). Using the turbulent heat fluxes computed from the sonic anemometers at 0.5 and 3.0 m AGL and accounting for humidity effects (Kaimal and Gaynor 1991), we estimate an upper bound error of 6 W m^{-2} due to the heat flux divergence. Direct measurements of radiative flux divergence at FLR (Hoch and Whiteman 2007) between 0.5 and 2 m AGL showed small values within $\pm 1 \text{ W m}^{-3}$ between 1500 and 1700 MST. The ground heat flux is generally underestimated (Oncley et al. 2007) since it is measured within the soil and corrected by means of soil temperature measurements above the ground heat flux plate. This error is especially important around local

sunset, when a strong temperature change is produced in the upper soil layer because of the rapid changes in the surface radiation budget. We estimate the maximum error made in the present case at $15\text{--}30\text{ W m}^{-2}$, based on a comparison with an alternative correction in which the thermal infrared surface temperature is substituted for the temperature of the soil layer. The sum of all these effects accounts, at maximum, for 80% of the residual. The rest of the energy imbalance may be attributed to advective effects caused by the slope current.

To describe the mechanisms involved in the onset of the downslope current during the evening transition, we have calculated the observed along-slope and cross-slope bulk momentum and buoyancy deficits of the slope current given by

$$UH = \int_0^h u \, dn, \quad (1)$$

$$VH = \int_0^h v \, dn, \quad \text{and} \quad (2)$$

$$\Delta\Theta H = g \int_0^h \frac{\Delta\theta}{\theta_0} \, dn, \quad (3)$$

where the upper limit of integration h ($=5\text{ m}$) is the highest level with measurements at the WU tower. The u and v components follow the local downslope (s) and cross-slope (y) directions. The downslope direction is 88° and 70° at WU and WL, respectively. The vertical velocity is perpendicular (n) to the underlying surface. Here, the temperature perturbation is defined as $\Delta\theta = \theta_0 - \theta$ so that it becomes a positive quantity for a denser fluid, which drives the current downslope. Since the main part of the temperature inversion is constrained within the first 5 m AGL (see previous section), the potential temperature of the undisturbed background field θ_0 is approximated here as the value at 5 m AGL for each tower. The evolution of these variables is shown in Fig. 10 for 1-min-averaged data at WU and WL during the evening period.

The defined bulk quantities are based on the model proposed by Manins and Sawford (1979). The along-slope momentum flux UH and cross-slope momentum flux VH reflect the evolution of the flow within the layer measured by the west slope towers, which is affected by a bulk buoyancy deficit $\Delta\Theta H$. However, these variables only describe the lowest 5 m of the flow. Anabatic flows have a depth larger than the tower heights (Serafin and Zardi 2010; Catalano and Cenedese 2010), as seen by the plume from the first smoke release, which was sporadically dispersed upward to the rim level. Tethersonde measurements over the east and west sidewalls indicate

an upslope direction of the flow throughout the entire crater depth (not shown). For the downslope regime, the depth of the current is uncertain, since a jetlike structure is not present below the heights of the towers and the wind measurements from the tethersondes are strongly variable near the surface.

The upslope regime is characterized by variable but mainly negative values of UH (upslope) at both towers and includes the *transition period* (1505–1540 MST), defined here as the time interval between a rapid increase of the buoyancy deficit at WU, which turns positive, and the final onset of the downslope current. The buoyancy deficit keeps growing at both sites and becomes positive at WL with the onset of the downslope flow, when both along-slope momentum fluxes reverse their signs. After a period with large values, the momentum fluxes reach a steady state between 1555 and 1710 MST. During this period, VH is positive at both sites, indicating that the downslope current is deviated northward with respect to the local slope. The buoyancy deficit grows at a faster rate at WL, reaching values larger than at WU because of the formation of a stronger temperature inversion at the lower part of the sidewall. In both cases, the buoyancy deficit stops growing after local sunset at FLR.

Figure 10 shows that the buoyancy deficit tends to push the air downslope at the upper sidewall, where the shadow arrives first, while the convective regime is still present at the lower sidewall. Nevertheless, once the flow is established—nearly simultaneously at both sites—the downslope momentum flux is greater at the lower sidewall than at the upper sidewall. This scenario is in contrast to the previous reports of upslope–downslope flow transitions (Hunt et al. 2003; Papadopoulos and Helmis 1999; Nadeau et al. 2013) or within valleys (Catalano and Cenedese 2010).

Hunt et al. (2003) analyze the flow transition considering that the cutoff of heating occurs at the same time over the slope and valley. In this context, the airflow still moves upslope because of its significant mean momentum. Papadopoulos and Helmis (1999) describe the formation of the downslope current without the presence of a previous upslope current, while Catalano and Cenedese (2010) perform a simulation where the sensible heat flux reverses first at the valley floor and then over the slope. A similar situation is observed by Nadeau et al. (2013) on a west-facing valley slope, where the shadow propagates up the slope, causing the downslope flow to start first at the lowest stations and then move up the slope. The upward shadow propagation is the exact opposite of our observations on the east-facing sidewall of the Meteor Crater, where the shadow moves down the slope (Fig. 3). This is reflected in the buoyancy deficit, which

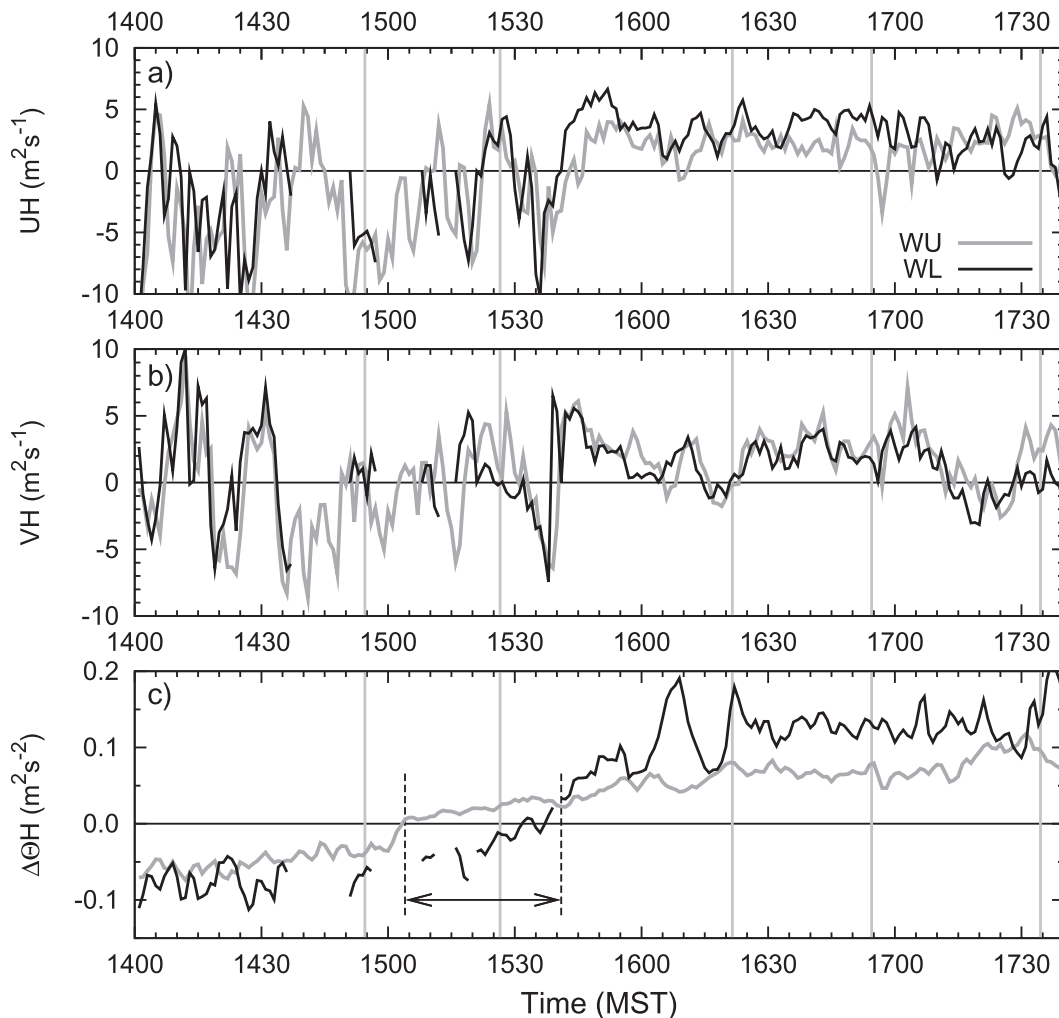


FIG. 10. Time evolution of the bulk (a) along-slope momentum flux (negative values indicate upslope flow), (b) cross-slope momentum flux, and (c) buoyancy deficit for the WU and WL sites during the upslope–downslope flow transition. Gray vertical lines are as in Fig. 6. In (c), the arrow indicates the transition period. The downslope direction is 88° and 70° at WU and WL, respectively. See text for reference.

first becomes positive at WU (Fig. 10), although the downslope flow starts almost at the same time at both slope sites, but later on the basin floor. In the present study, the interaction between the buildup of the stably stratified layer over the west sidewall and the convective regime at the crater floor and east sidewall are thus key to understanding the upslope–downslope flow transition.

The presence of the upslope current over the sidewall leads to strong turbulence close to the ground (Fig. 9), contributing to a large heat exchange at the surface and cooling of the surface layer during the transition period on the upper sidewall. This cooling process, however, is mostly balanced by the advection of warmer air coming from the valley floor carried by the anabatic or upslope current.

Considering the temperature tendency equation

$$\frac{\partial \theta}{\partial t} + \mathbf{v} \cdot \nabla \theta = -\frac{1}{\rho_0 C_p} \frac{\partial R_n}{\partial z} - \frac{\partial \overline{w'\theta'}}{\partial z}, \quad (4)$$

with the vertical flux divergences of net radiation R_n and kinematic heat flux $\overline{w'\theta'}$, it is possible to estimate the contribution of advection. The layer between 0.5 and 5 m at WU was cooled at the rate of 3.5 K h^{-1} during the transition period because of turbulent heat flux divergence. However, the total cooling rate of the layer during this period was 0.6 K h^{-1} . Thus, the advective term should be 2.9 K h^{-1} to balance Eq. (4). Assuming a scale velocity of 1 m s^{-1} , there should be a temperature difference of 0.1 K between WU and WL, which are

separated by approximately 130 m. The advection term may be larger, since we have not accounted for the contribution of the radiative term. Sun et al. (2003) identified radiative flux divergence in the lowest 50 m as a contributing factor in the cooling process in the late afternoon. Direct observations of radiative flux divergence at FLR (Hoch and Whiteman 2007) show a transition from radiative heating to cooling at about 1600 MST. In any case, these estimates are compatible with temperature differences between WU and WL, as shown in Fig. 7.

To assess which forcings contribute to the evolution of UH and VH, the along-slope and cross-slope momentum equations over the sidewall can be written using the Boussinesq approximation, as

$$\frac{\partial u}{\partial t} + \mathbf{v} \cdot \nabla u = -\frac{1}{\rho_0} \frac{\partial(\Delta p)}{\partial s} - g \frac{\Delta \theta}{\theta_0} \sin \alpha + \frac{\partial \tau_u}{\partial n} \quad (5)$$

and

$$\frac{\partial v}{\partial t} + \mathbf{v} \cdot \nabla v = -\frac{1}{\rho_0} \frac{\partial(\Delta p)}{\partial y} + \frac{\partial \tau_v}{\partial n}, \quad (6)$$

where the evolution of the downslope momentum and the advection in Eq. (5) is related to the perturbation pressure gradient force, the along-slope buoyancy force, and the shear stress τ_u . The slope angle is given by α . The cross-slope momentum equation [Eq. (6)] does not include the buoyancy force, since the y direction is perpendicular to this force. The time derivative of the curves in Figs. 10a and 10b represent the bulk version of the first term on the lhs of Eqs. (5) and (6). The terms of these budget equations are discussed to provide a tentative qualitative description of the upslope–downslope flow transition.

During the convective regime, the wavelet transform analysis shows the presence of time scales related to the crater size, connecting the upslope current with larger circulations driven by the convection. Under this situation, the anabatic current probably draws in flow from higher-level air, forming a recirculating flow typical of alpine-like valleys. Thus, the advective and pressure gradient terms also contribute to the evolution of UH and VH.

During the transition period, a diabatic cooling process starts at WU, forming a surface temperature inversion. During this stage, the atmosphere experiences rapid changes over the upper-west sidewall, with the buoyancy force changing its sign and introducing a downslope contribution. In this transient situation, the pressure perturbation field probably takes either sign, compensating or contributing to the buoyancy forcing. Advective terms are responsible for compensating these previous forces, as the air still blows upslope.

The convective regime ceases abruptly with a large energetic event, which is seen everywhere at all crater scales (Fig. 9). This is followed by the onset of the downslope wind at WL and, two minutes later, WU, which starts as a southerly flow (note the positive value in VH) and progressively veers toward a downslope direction. At both towers, the onset of the downslope flow coincides with a sudden shift of wind direction and a drop in air temperature (Fig. 7). This suggests the hypothesis that the downslope flow is initiated by the arrival of a gravity current from the cold area located at the southwestern sidewall. A southerly wind component is also observed at all other sites throughout the crater at approximately the same time, starting on the east sidewall and propagating westward (not shown). This points to a second hypothesis, namely that the southerly wind component that occurs before the transition on the west sidewall is not directly related to the onset of the downslope flow.

Once the large eddies from the convective regime disappear in the western part of the crater, buoyancy force drives the air over the sidewall in a downslope direction. The air follows the terrain slope close to the surface, but it is deviated toward a southwesterly direction with height (Figs. 6g,h). At a crater scale, the southwest–northeast axis is the direction of the largest thermal gradient between opposing sidewalls because of the differential heating rates during the late afternoon (Fig. 3), which gives rise to cross-basin flows in the direction of the thermal gradient (Lehner et al. 2011). Haiden and Whiteman (2005) and Mahrt et al. (2001) note that katabatic flows follow topographic gradients of a larger scale at higher levels. Similarly, in the present case, the drainage current would be sensitive to the thermal gradient at the crater scale for increasing heights, where the buoyancy deficit is small. At WU, the difference between the aspect angle and the temperature gradient direction at the crater scale is larger than at WL, producing a stronger wind direction shear. This thermal gradient at the crater scale may be reflected in the pressure perturbation term of the cross-slope momentum equation in Eq. (6). For the along-slope direction [Eq. (5)], however, the pressure gradient term probably becomes smaller, since the basin temperature inversion is not formed yet and, consequently, the pressure perturbation does not change significantly down the slope (Zhong and Whiteman 2008).

An estimation of the terms of Eq. (5) for the steady period of downslope flow (1555–1710 MST) show that buoyancy and friction terms compensate the advection terms, resembling the features of a shooting flow, as classified by Mahrt (1982). The along-slope pressure gradient term is small, as well as the residual of the momentum budget.

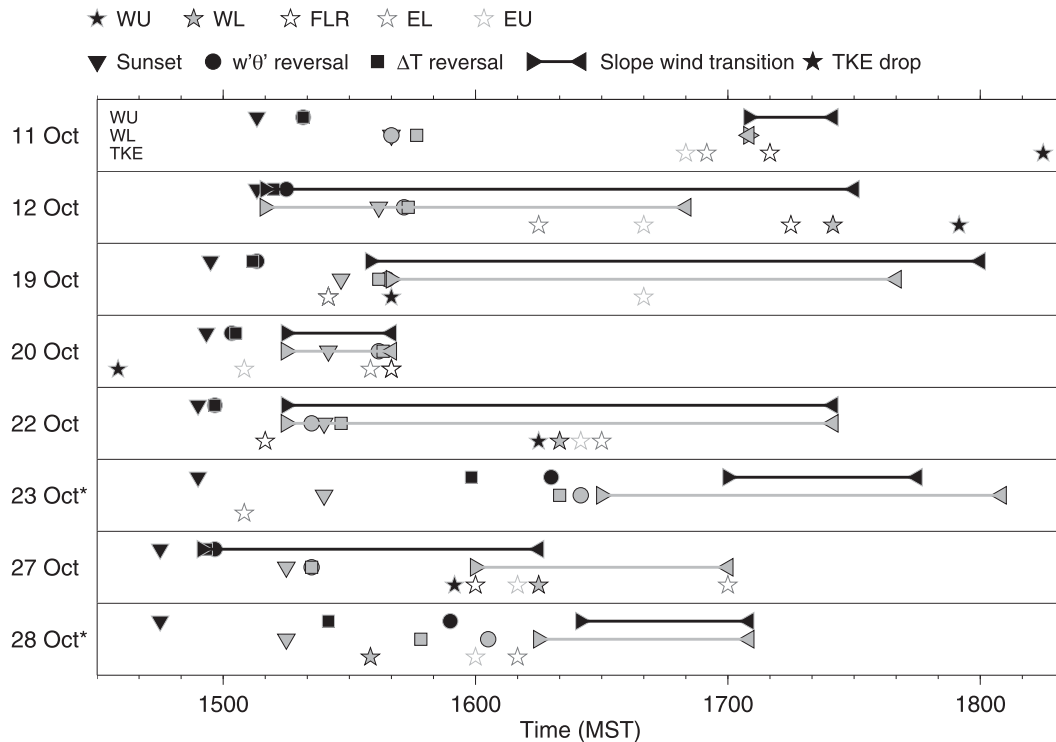


FIG. 11. Times of local sunset, $\overline{w'\theta'}$ reversal at 5 m AGL, ΔT reversal between 5 and 1.5 m AGL, and the upslope–downslope transition period at WU and WL and times when TKE at 5 m AGL finally drops below $1 \text{ m}^2 \text{ s}^{-2}$ during the upslope–downslope transition period at WU, WL, FLR, EL, and EU for eight selected days. Times of sunset, $\overline{w'\theta'}$ reversal, and ΔT reversal were determined from 30-s-averaged data; the wind transition was determined from 10-min running means of 30-s-averaged data; and TKE was calculated from 5-min-averaged data. Local sunset was determined from incoming shortwave radiation. Days with clouds in the afternoon are marked with an asterisk; time of local sunset on each of these days was determined from incoming radiation on the previous day.

7. Comparison with other days

Observations from several other days of the one-month-long field campaign show similarities to the upslope–downslope transition on 20 October in terms of timing and development. But there were also day-to-day variations supporting the idea that the transition is not solely influenced by the local energy budget. We identified seven additional days with relatively well-defined upslope–downslope flow transitions on the west sidewall. The temporal evolution of the transition on the seven days and on the previously discussed 20 October is summarized in Fig. 11. Time series of the slope winds in the late afternoon on five of the selected days are shown in Fig. 12 together with time series of TKE and $\overline{w'\theta'}$. All eight nights were categorized as fully decoupled from the ambient atmosphere by Yao and Zhong (2009), meaning that a strong inversion formed in the crater during these nights. However, on two of the selected days it was cloudy in the afternoon (i.e., 23 and 28 October). A short overview of the synoptic situation during the entire month of October can be found in Whiteman et al. (2008).

Local sunset at WU and WL changes by ~ 25 min between 11 and 28 October and sunset at WL occurs always approximately 30 min after sunset at WU (Fig. 11). The sign of the heat flux $\overline{w'\theta'}$ at both sites reverses generally within about 5–15 min after local sunset. The heat flux oscillates around 0 K m s^{-1} at the time of reversal so that the exact time of reversal is difficult to determine, so the times indicated in Fig. 11 are our best estimates. Except for the cloudy days, ΔT between 5 and 1.5 m AGL reverses its sign almost simultaneously with the reversal of $\overline{w'\theta'}$, marking the beginning of nighttime stability in the near-surface layer.

On 11 October, $\overline{w'\theta'}$ at WU and WL reverses at 1519 and 1540 MST, respectively, that is, just a few minutes after local sunset (Figs. 11 and 12). The transition from upslope to downslope winds, however, occurs about 1.5 h later. At WL, a sharp transition from a southeasterly to a westerly direction is observed at 1705 MST. At WU, the complete transition takes slightly longer, lasting from 1705 to 1725 MST. It has to be noted that the transition periods shown in Fig. 11 were determined subjectively based on time series of wind direction as the

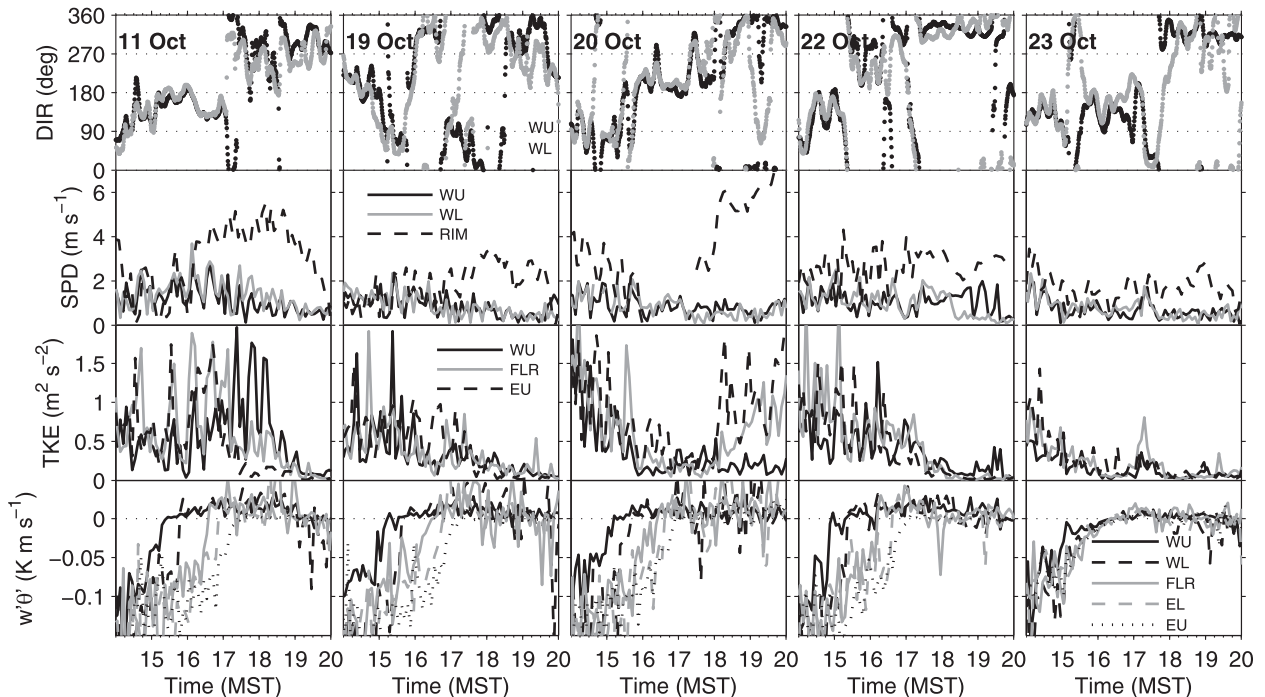


FIG. 12. (top) Time series of wind direction at WU and WL; (top middle) wind speed at WU, WL, and RIM; (bottom middle) TKE at WU, FLR, and EU; and (bottom) $w'\theta'$ at WU, WL, FLR, EL, and EU for 11, 19, 20, 22, and 23 Oct. Wind direction, TKE, and $w'\theta'$ are 5-min averages; wind direction is a 10-min running mean of 30-s-averaged data. Wind speed at RIM is at 10 m AGL; all other data are at 5 m AGL.

time period of variable wind direction between a relatively constant south-southeasterly upslope flow and a westerly downslope flow. During the time period between the local sunset and the onset of the downslope current on the west sidewall, TKE is relatively high at FLR and on the east sidewall ($1\text{--}2\text{ m}^2\text{ s}^{-2}$; Fig. 12) when compared with the case analyzed on 20 October. A sudden drop in TKE at EU and FLR between 1640 and 1710 MST is followed by an increase of TKE on the west sidewall with the onset of the downslope flow. Besides, this time also agrees with a wind shift at RIM to an east-northeasterly direction (not shown) and with relatively high wind speeds of about 4 m s^{-1} (Fig. 12), which means that a dynamic contribution to the downslope flow cannot be entirely ruled out in this case.

Upslope–downslope transitions, which start shortly after local sunset on the west sidewall similar to 20 October, are also observed on 12, 19, 22, and 27 October (Fig. 11). On 12 and 22 October the transition at both WU and WL starts even before local sunset at WL. But slope winds generally remain variable until TKE decreases, similar to observations from 11 October. On 19 October, the transition from an easterly upslope flow to a westerly downslope flow starts almost simultaneously with the reversal of ΔT at WL, but the winds on the west sidewall stay variable until approximately

1740–1800 MST (Fig. 12). TKE is relatively low throughout the afternoon but the final drop to values below $0.5\text{ m}^2\text{ s}^{-2}$ occurs at 1730 MST at FLR and on the east sidewall. This is significantly later compared to 20 October, when TKE at all sites drops below this threshold before 1645 MST. On 22 October, slope winds remain variable until approximately 1725 MST. TKE decreases at FLR and on the east sidewall shortly after 1500 MST before the beginning of the transition on the west sidewall (Fig. 12). But the final drop in TKE below $0.5\text{ m}^2\text{ s}^{-2}$ occurs at all sites in the crater around 1715 MST.

On 23 October, the transition is strongly influenced by the presence of clouds in the afternoon. The heat flux decreases very slowly and simultaneously at WU and WL, reversing at approximately 1625 MST (Figs. 11 and 12). It then becomes only weakly positive compared to the other days. Consequently, the layer over the west slope stabilizes at or after 1600 MST. This is also reflected in the transition from upslope to downslope winds, which starts relatively late. A continuous downslope flow is not present until 1745 and 1805 MST at WU and WL, respectively. A similar development is observed on 28 October, which is also cloudy in the afternoon (Fig. 11).

The development of the transition from upslope to downslope flow on the west crater sidewall on these

seven days agrees with the case study from 20 October insofar as the transition seems to depend strongly but not exclusively on the local energy budget on the west sidewall. Large-scale motions in the remainder of the crater atmosphere seem to affect the duration of the transition from upslope to downslope winds. This is indicated by the apparent connection to TKE throughout the basin. Slope winds on the west sidewall tend to stay variable after local sunset and after the beginning of the transition period until daytime convection subsides and TKE decreases. However, if TKE stays relatively high after local sunset (e.g., 11 October), the transition on the west sidewall is delayed. This effect may be the result of a dynamic contribution from the ambient atmosphere, since the wind speed at the crater rim exceeds 4 m s^{-1} for these cases. The small size of the Meteor Crater generates circulations of different spatial scales that interact strongly and may be responsible for the day-to-day variations observed. An interesting difference to previous studies is the almost simultaneous flow transition at WU and WL, which was observed on some days. This could be related to the impact of TKE and daytime convection on the timing of the transition.

8. Conclusions

The evening transition in the Meteor Crater basin is strongly influenced by the propagation of shadows, which induce the development of a stable layer over the west sidewall while the sun still heats the surface over the eastern part of the crater. This situation leads to temperature differences within the crater atmosphere between the opposing sidewalls, and also to the upslope–downslope flow transition over the west sidewall. This flow transition was observed during the late afternoon of 20 October 2006 with three smoke releases over the west sidewall.

The downslope propagation of a shadow cast from the western rim of the crater leads to a sudden drop of net radiation as the terminator passes. Radiative cooling of the ground causes the near-surface air temperature to decrease and reverses the turbulent sensible heat flux in the near-surface air layer. A measured imbalance in the surface energy budget at this time is apparently caused primarily by uncertainty in the ground heat flux measurements and advection of warmer air by the upslope–downslope current.

The cooling process at the upper part of the sidewall is driven by flux divergences of the sensible heat and net radiation, but it is partially counteracted by the warm advection produced by the anabatic current.

Results from a wavelet transform suggest that the upslope–downslope flow transition is driven by motions

with a range of scales up to crater size, probably connected with closed circulation patterns similar to those usually found in alpine valleys. The progressive buildup of stability over the west sidewall leads to the formation of a positive buoyancy force, which, after storing enough potential energy, is able to counteract these circulation patterns. The sudden change in the local dynamics is preceded by a peak of energy at all scales throughout the crater, which is detected by the sonic anemometers right before the onset of the downslope current. This evolution contrasts with the turbulence decay over flat terrain where convection gradually subsides as the surface heat flux decreases.

The downslope regime starts with a southerly flow at both west slope towers, veering to a southwest direction 10 min later. It is characterized by a stable layer carrying cold air from the southwest sidewall. Wind direction also shows a layering effect, following the surface at lower levels, but blowing in the direction of the largest thermal gradient between opposing sides of the crater at higher levels. The wind direction shear produces turbulence close to the ground, enhancing the surface heat exchange. The scale of this motion is also reflected in the wavelet transform results, giving a maximum contribution from time scales around 12 min.

The downslope current arrives at the center of the crater floor 10 min after its onset over the west sidewall, cooling the area before local sunset. However, the formation of a strong surface temperature inversion follows the arrival of the shadow. The downslope current reaches a steady regime for approximately two hours, completing the buildup of the cold pool on the crater floor.

An analysis of the forcings involved in the upslope–downslope flow transition suggests that the growth of the buoyancy force at the upper part of the slope is counteracted by the advection of the anabatic current. Once the drainage current is established, the pressure perturbation directs the downslope flow toward the warmer sidewall.

In addition to the case study of 20 October, the upslope–downslope transition was analyzed for seven other days. A relatively late transition occurs on cloudy afternoons, when the heat flux reverses late and simultaneously on the whole west sidewall since the influence of the shadow propagation is not present. On clear-sky days, the transition is initiated shortly after local sunset on most of the days but a constant downslope wind is not established until TKE decreases on the crater floor and the east sidewall, indicating the end of strong daytime convection. When the wind speed outside the crater is large enough, a dynamical contribution from the ambient atmosphere may delay the upslope–downslope transition on the west sidewall.

Acknowledgments. This paper, started while the first author was a visiting scientist at the University of Utah, was supported by a travel grant from the fellowship BES-2007-16272 of the research project CGL2006-12474-C03-01, together with the research projects CGL2009-12797-C03-01 and CGL2012-37416-C04-01, all from the Spanish government. Contributions by the coauthors were supported by National Science Foundation Grants ATM-0444205 and AGS-1160730 (CDW and ML), by Army Research Office Grant 52734-EV (SWH), and by a DOC-ffORTE fellowship from the Austrian Academy of Sciences (ML). We thank the Barringer Crater Company (D. Barringer, president) and Meteor Crater Enterprises, Inc. (B. Andes, president), for crater access, and those listed in the acknowledgments section of Whiteman et al. (2008) for their help with the field program and data processing. Chad Kahler is thanked for assistance with Figure 3. Marta Jordi is acknowledged for valuable comments on the first draft of the manuscript. Two anonymous reviewers have provided very useful comments that have contributed to the improvement of the paper.

REFERENCES

- Brazel, A. J., H. J. S. Fernando, J. C. R. Hunt, N. Selover, B. C. Hedquist, and E. R. Pardyjak, 2005: Evening transition observations in Phoenix, Arizona. *J. Appl. Meteor.*, **44**, 99–112.
- Catalano, F., and A. Cenedese, 2010: High-resolution numerical modeling of thermally driven slope winds in a valley with strong capping. *J. Appl. Meteor. Climatol.*, **49**, 1859–1880.
- Clements, C. B., C. D. Whiteman, and J. D. Horel, 2003: Cold-air-pool structure and evolution in a mountain basin: Peter Sinks, Utah. *J. Appl. Meteor.*, **42**, 752–768.
- , W. Yao, S. Zhong, C. D. Whiteman, and T. Horst, 2007: Slope flows observed during METCRAX. *Extended Abstracts, 29th Int. Conf. on Alpine Meteorology (ICAM)*, Chambéry, France, Météo France, 2D.7. [Available online at http://www.cnr.meteo.fr/icam2007/ICAM2007/extended/manuscript_105.pdf.]
- Cuxart, J., G. Morales, E. Terradellas, and C. Yagüe, 2002: Study of coherent structures and estimation of the pressure transport terms for the nocturnal stable boundary layer. *Bound.-Layer Meteor.*, **105**, 305–328.
- , M. A. Jiménez, and D. Martínez, 2007: Nocturnal meso-beta and katabatic flows on a midlatitude island. *Mon. Wea. Rev.*, **135**, 918–932.
- Fast, J., S. Zhong, and C. D. Whiteman, 1996: Boundary layer evolution within a canyonland basin. Part II: Numerical simulations of nocturnal flows and heat budgets. *J. Appl. Meteor.*, **35**, 2162–2178.
- Fernando, H. J. S., B. Verhoef, S. Di Sabatino, L. S. Leo, and S. Park, 2013: The Phoenix Evening Transition Flow Experiment (TRANSFLEX). *Bound.-Layer Meteor.*, **147**, 443–468, doi:10.1007/s10546-012-9795-5.
- Fleagle, R. G., 1950: A theory of air drainage. *J. Meteor.*, **7**, 227–232.
- Goulart, A., B. Bodmann, M. de Vilhena, P. Soares, and D. Moreira, 2010: On the time evolution of the turbulent kinetic energy spectrum for decaying turbulence in the convective boundary layer. *Bound.-Layer Meteor.*, **138**, 61–75.
- Haiden, T., and C. D. Whiteman, 2005: Katabatic flow mechanisms on a low-angle slope. *J. Appl. Meteor.*, **44**, 113–126.
- Heinemann, G., 2002: Modelling and observations of the katabatic flow dynamics over Greenland. *Tellus*, **54A**, 542–554.
- Hoch, S. W., and C. D. Whiteman, 2007: Observations of radiative flux divergence and vertical temperature structure evolution. *24th General Assembly, Int. Union of Geodesy and Geophysics*, Perugia, Italy, IUGG, P5003. [Available online at http://www.inscc.utah.edu/~whiteman/METCRAX/images/lwdiv_poster_IUGG.pdf.]
- , and —, 2010: Topographic effects on the surface radiation balance in and around Arizona's Meteor Crater. *J. Appl. Meteor. Climatol.*, **49**, 1114–1128.
- Horst, T. W., and D. H. Lenschow, 2009: Attenuation of scalar fluxes measured with spatially-displaced sensors. *Bound.-Layer Meteor.*, **82**, 219–233.
- Hunt, J. C. R., H. J. S. Fernando, and M. Princevac, 2003: Unsteady thermally driven flows on gentle slopes. *J. Atmos. Sci.*, **60**, 2169–2182.
- Kaimal, J. C., and J. E. Gaynor, 1991: Another look at sonic thermometry. *Bound.-Layer Meteor.*, **56**, 401–410.
- Kring, D. A., 2007: *Guidebook to the Geology of Barringer Meteorite Crater, Arizona (a.k.a. Meteor Crater)*. LPI Contribution 1355, Lunar and Planetary Institute, Houston, TX, 150 pp.
- Lehner, M., and C. D. Whiteman, 2012: The thermally driven cross-basin circulation in idealized basins under varying wind conditions. *J. Appl. Meteor. Climatol.*, **51**, 1026–1045.
- , —, and S. W. Hoch, 2011: Diurnal cycle of thermally driven cross-basin winds in Arizona's Meteor Crater. *J. Appl. Meteor. Climatol.*, **50**, 729–744.
- Mahrt, L., 1982: Momentum balance of gravity flows. *J. Atmos. Sci.*, **39**, 2701–2711.
- , and S. Larsen, 1982: Small scale drainage flow. *Tellus*, **34**, 579–587.
- , D. Vickers, R. Nakamura, M. R. Soler, J. L. Sun, S. Burns, and D. H. Lenschow, 2001: Shallow drainage flows. *Bound.-Layer Meteor.*, **101**, 243–260.
- , S. Richardson, N. Seaman, and D. Stauffer, 2010: Non-stationary drainage flows and motions in the cold pool. *Tellus*, **62A**, 698–705.
- Manins, P. C., and B. L. Sawford, 1979: A model of katabatic winds. *J. Atmos. Sci.*, **36**, 619–630.
- Martínez, D., and J. Cuxart, 2009: Assessment of the hydraulic slope flow approach using a mesoscale model. *Acta Geophys.*, **57**, 882–903.
- McNider, R. T., 1982: A note on velocity fluctuations in drainage flows. *J. Atmos. Sci.*, **39**, 1658–1660.
- Meyers, S. D., B. G. Kelly, and J. J. O'Brien, 1993: An introduction to wavelet analysis in oceanography and meteorology: With application to the dispersion of Yanai waves. *Mon. Wea. Rev.*, **121**, 2858–2866.
- Monti, P., H. J. S. Fernando, M. Princevac, W. C. Chan, T. A. Kowalewski, and E. R. Pardyjak, 2002: Observations of flow and turbulence in the nocturnal boundary layer over a slope. *J. Atmos. Sci.*, **59**, 2513–2534.
- Nadeau, D. F., E. R. Pardyjak, C. W. Higgins, H. J. S. Fernando, and M. B. Parlange, 2011: A simple model for the afternoon and early evening decay of convective turbulence over different land surfaces. *Bound.-Layer Meteor.*, **141**, 301–324.
- , —, —, H. Huwald, and M. B. Parlange, 2013: Flow during the evening transition over steep Alpine slopes. *Quart. J. Roy. Meteor. Soc.*, **139**, 607–624.

- Oncley, S. P., and Coauthors, 2007: The energy balance experiment EBEX-2000. Part I: Overview and energy balance. *Bound.-Layer Meteor.*, **123**, 1–28.
- Papadopoulos, K. H., and C. G. Helmis, 1999: Evening and morning transition of katabatic flows. *Bound.-Layer Meteor.*, **92**, 195–227.
- , —, A. T. Soilemes, J. Kalogiros, P. G. Papageorgas, and D. N. Asimakopoulos, 1997: The structure of katabatic flows down a simple slope. *Quart. J. Roy. Meteor. Soc.*, **123**, 1581–1601.
- Prandtl, L., 1942: *Führer durch die Strömungslehre (Essentials of Fluid Mechanics)*. Vieweg und Sohn, 382 pp.
- Renfrew, I. A., 2004: The dynamics of idealized katabatic flow over a moderate slope and ice shelf. *Quart. J. Roy. Meteor. Soc.*, **130**, 1023–1045.
- Schotanus, P., F. T. M. Nieuwstadt, and H. A. R. DeBruin, 1983: Temperature measurement with a sonic anemometer and its application to heat and moisture fluctuations. *Bound.-Layer Meteor.*, **26**, 81–93.
- Serafin, S., and D. Zardi, 2010: Structure of the atmospheric boundary layer in the vicinity of a developing upslope flow system: A numerical model study. *J. Atmos. Sci.*, **67**, 1171–1185.
- Simpson, J. E., 1999: *Gravity Currents in the Environment and the Laboratory*. 2nd ed. Cambridge University Press, 259 pp.
- Sorbjan, Z., 1997: Decay of convective turbulence revisited. *Bound.-Layer Meteor.*, **82**, 503–517.
- Sun, J., S. P. Burns, A. C. Delany, S. P. Oncley, T. W. Horst, and D. H. Lenschow, 2003: Heat balance in the nocturnal boundary layer during CASES-99. *J. Appl. Meteor.*, **42**, 1649–1666.
- van Dijk, A., W. Kohsiek, and H. A. R. DeBruin, 2003: Oxygen sensitivity of krypton and Lyman- α hygrometers. *J. Atmos. Oceanic Technol.*, **20**, 143–151.
- Viana, S., C. Yagüe, and G. Maqueda, 2009: Propagation and effects of a mesoscale gravity wave over a weakly-stratified nocturnal boundary layer during the SABLES2006 field campaign. *Bound.-Layer Meteor.*, **133**, 165–188.
- , E. Terradellas, and C. Yagüe, 2010: Analysis of gravity waves generated at the top of a drainage flow. *J. Atmos. Sci.*, **67**, 3949–3966.
- Webb, E. K., G. I. Pearman, and R. Leuning, 1980: Correction of flux measurements for density effects due to heat and water vapor transfer. *Quart. J. Roy. Meteor. Soc.*, **106**, 85–100.
- Whiteman, C. D., 2000: *Mountain Meteorology: Fundamentals and Applications*. Oxford University Press, 355 pp.
- , K. J. Allwine, L. J. Fritschen, M. M. Orgill, and J. R. Simpson, 1989: Deep valley radiation and surface energy budget microclimates. Part II: Energy budget. *J. Appl. Meteor.*, **28**, 427–437.
- , and Coauthors, 2008: METCRAX 2006—Meteorological experiments in Arizona’s Meteor Crater. *Bull. Amer. Meteor. Soc.*, **89**, 1665–1680.
- , S. W. Hoch, M. Lehner, and T. Haiden, 2010: Nocturnal cold-air intrusions into a closed basin: Observational evidence and conceptual model. *J. Appl. Meteor. Climatol.*, **49**, 1894–1905.
- Wilczak, J. M., S. P. Oncley, and S. A. Stage, 2001: Sonic anemometer tilt correction algorithms. *Bound.-Layer Meteor.*, **99**, 127–150.
- Yao, W., and S. Zhong, 2009: Nocturnal temperature inversions in a small, enclosed basin and their relationship to ambient atmospheric conditions. *Meteor. Atmos. Phys.*, **103**, 195–210.
- Zardi, D., and C. D. Whiteman, 2012: Diurnal mountain wind systems. *Mountain Weather Research and Forecasting*, F. K. Chow, S. F. J. DeWekker, and B. Snyder, Eds., Springer, 35–119.
- Zhong, S., and C. D. Whiteman, 2008: Downslope flows on a low-angle slope and their interactions with valley inversions. Part II: Numerical modeling. *J. Appl. Meteor. Climatol.*, **47**, 2039–2057.